SENSITIVITY ANALYSIS OF ELASTIC FULL-WAVEFORM INVERSION FOR ORTHORHOMBIC MEDIA

SAGAR SINGH and ILYA TSVANKIN

Center for Wave Phenomena, Colorado School of Mines, Golden, CO 80401, U.S.A. sagarsinghiitr16@gmail.com, ilya.tsvankin@gmail.com

ABSTRACT

Singh, S. and Tsvankin, I., 2022. Sensitivity analysis of elastic full-waveform inversion for orthorhombic media. *Journal of Seismic Exploration*, 31: 105-130.

Application of elastic full-waveform inversion (FWI) to orthorhombic models, which are typical for many subsurface formations, is highly challenging due to the large computational cost and parameter trade-offs. Analyzing radiation (scattering) patterns of the medium parameters can yield valuable insights into potential trade-offs and the types of data required for reliable parameter estimation. These patterns can be obtained by computing the seismic wavefield due to parameter perturbations represented by the sensitivity kernels (the Fréchet derivatives). We study the sensitivity of FWI to the parameters of elastic orthorhombic media by examining the radiation patterns for a background VTI (transversely isotropic with a vertical axis of symmetry) model. The employed velocity-based parameterization, which represents an extension of previously published notations, can be efficiently incorporated into the FWI framework. In contrast to most existing publications, our analysis includes the radiation patterns for a perturbation in density. The results show that the vertical velocities of the S-waves and the symmetry-direction horizontal velocities of the P-waves can be obtained with high resolution from P- and PS-wave reflection data. The patterns for the S-wave vertical velocities, however, have some overlap with those for the P-wave normal-moveout (NMO) velocities. The P-wave vertical velocity can also be resolved from the pure P and converted PSV reflections but the estimation of the SH-wave symmetry-direction horizontal velocity requires the acquisition of pure shear data. The radiation-pattern analysis also shows that it may be possible to constrain density by inverting the pure-mode P- and S-waves. To verify the conclusions of the sensitivity analysis, we perform FWI of the vertical displacement generated for two horizontal orthorhombic layers beneath a VTI overburden.

KEY WORDS: full-waveform inversion, anisotropy, orthorhombic symmetry, elastic media, multicomponent data, radiation patterns.

INTRODUCTION

Orthorhombic models are often required to properly image azimuthally anisotropic formations in such regions as the Gulf of Mexico (Li et al., 2012; Herrera et al., 2014; Xie et al., 2017) and to estimate the parameters of fractured reservoirs (Bakulin et al., 2000b; Tsvankin and Grechka, 2011; Maitra et al., 2018; Masmoudi and Alkhalifah, 2018). Therefore, it is becoming increasingly important to build robust orthorhombic velocity models from reflection seismic data.

Full-waveform inversion (FWI) has been successfully used to reconstruct subsurface velocity fields with high spatial resolution. Elastic FWI, despite its large computational cost, is particularly promising for multiparameter anisotropic models because it can operate with multicomponent data and properly handle reflection amplitudes. A crucial step in FWI is efficient computation of the inversion gradient, which is typically carried out using the adjoint-state method rather than the first-order partial-derivative wavefields, also called the Fréchet derivatives (e.g., Liu and Tromp, 2006; Singh et al., 2018). An approximate Hessian matrix needed for Gauss-Newton optimization can be calculated from the second partial-derivative wavefields (e.g., Pratt et al., 1998).

The Fréchet derivatives, however, can provide valuable information for sensitivity analysis in FWI because they can be interpreted as the wavefield responses produced by perturbations of the model parameters. The amplitude variation of the Fréchet derivatives with the scattering angle (so-called radiation or sensitivity patterns) reveals a close relationship between AVO (amplitude-variation-with-offset) analysis and FWI (Oh and Alkhalifah, 2016). Studying the radiation patterns helps understand parameter trade-offs and guide model updates for multiparameter FWI.

Radiation-pattern analysis is particularly important for low-symmetry anisotropic models described by a large number of independent parameters, such as orthorhombic. The radiation patterns of different parameters often overlap, which helps identify parameter trade-offs (crosstalk) and devise strategies to mitigate them (Tarantola, 1986; Alkhalifah and Plessix, 2014).

The majority of existing studies for azimuthally anisotropic models focus on HTI (transversely isotropic with a horizontal axis of symmetry) media (e.g., Rüger, 1997; Bakulin et al., 2000a). The HTI model, which describes a single system of penny-shaped cracks embedded in a purely isotropic host rock, can be treated as a special case of the more realistic orthorhombic symmetry (Tsvankin, 1997). The forward-modeling problem for orthorhombic media is well studied in the literature (Schoenberg and Helbig, 1997; Tsvankin, 2012; Song and Alkhalifah, 2013; Ibanez-Jacome et. al., 2014). Parameter estimation, however, has been largely limited to piecewise-homogeneous orthorhombic models and based on moveout and

AVO inversion (Grechka and Tsvankin, 1999; Bakulin et al., 2000b; Vasconcelos and Tsvankin, 2006; Tsvankin and Grechka, 2011; Liu and Tsvankin, 2019). Although there are several publications on FWI for acoustic and elastic orthorhombic media (Wang and Tsvankin, 2018; Oh and Alkhalifah, 2019), development of efficient inversion algorithms for heterogeneous orthorhombic models remains challenging.

Here, we present explicit expressions for the Fréchet derivatives with respect to the parameters of orthorhombic media (including density) and study the corresponding radiation patterns. This sensitivity analysis should help in developing practical strategies for mitigating parameter trade-offs in elastic FWI for orthorhombic media. Previous studies of the radiation patterns for orthorhombic media are limited to a purely isotropic background (Pan et al., 2014; Moradi and Innanen, 2017, 2019; Kazei and Alkhalifah, 2019). Here, we evaluate the sensitivity of FWI to the parameters of an elastic orthorhombic perturbation embedded in a background VTI medium. We employ a velocity-based parameterization, which is particularly efficient for anisotropic elastic FWI (Kamath and Tsvankin, 2016; Singh et al., 2020, 2021). Furthermore, we analyze the radiation patterns for a perturbation in density - a parameter that is seldom updated in existing FWI algorithms.

We start by briefly discussing the general principles of elastic FWI including the gradient computation and parameter updating. Then we derive an approximation for the radiation patterns from an arbitrarily anisotropic perturbation by employing the concept of an equivalent body force (described by the moment tensor). The developed formalism is used to study the radiation patterns of the parameters of orthorhombic media and to evaluate the corresponding trade-offs. Finally, FWI of the vertical displacement records for a layered orthorhombic medium beneath a VTI overburden is carried out to assess the validity of the predictions based on the radiation patterns.

FWI METHODOLOGY

Most FWI algorithms employ the l^2-norm to minimize the least-squares distance between the observed ($\mathbf{u}^{\mathrm{obs}}$) and simulated ($\mathbf{u}^{\mathrm{sim}}$) wavefields:

$$E(\mathbf{m}) = \sum_{s=1}^{n_s} \left\| \mathbf{u}^{\mathrm{obs}} - \mathbf{X}\mathbf{u}^{\mathrm{sim}}(\mathbf{m}) \right\| \ , \tag{1}$$

where $E(\mathbf{m})$ is the objective function, n_s is the number of sources, $\mathbf{m}$ is the vector of model parameters, and $\mathbf{X}$ is an operator that generates the data at the receiver locations. Typically, the objective function is iteratively minimized using gradient-based algorithms.

Multiparameter inversion generally increases the nonlinearity of the inverse problem, and the objective function $E(\mathbf{m})$ may have a number of local minima. If the initial model lies in the proximity of the global minimum of E (basin of convergence), the inversion can be implemented via a local gradient-based approach:

$$\mathbf{m}^{(i+1)} = \mathbf{m}^{(i)} + \alpha^{(i)}\mathbf{P}^{(i)} \quad , \tag{2}$$

where $\mathbf{m}^{(i+1)}$ is the model-parameter vector at the i-th iteration, $\alpha^{(i)}$ is the step length, and $\mathbf{P}^{(i)}$ specifies the direction of model updating:

$$\mathbf{P} = \mathbf{H}^{-1}\mathbf{g} . \tag{3}$$

Here, the vector $\mathbf{g}$ (inversion gradient) and matrix $\mathbf{H}$ (Hessian) contain the first- and second-order partial derivatives of the objective function with respect to the model parameters. According to the adjoint-state method, the inversion gradient can be constructed by convolving the first-order partial-derivative wavefields with the complex conjugate of the data residuals (Tarantola, 1986):

$$\mathbf{g} = \left[\frac{\partial \mathbf{u}^{\text{sim}}}{\partial \mathbf{m}}\right]^T \left(\mathbf{u}^{\text{obs}} - \mathbf{X}\mathbf{u}^{\text{sim}}\right), \tag{4}$$

where $\partial \mathbf{u}^{\text{sim}}/\partial \mathbf{m}$ is the Fréchet derivative and T denotes the transpose operator. The Hessian matrix $\mathbf{H}$ (ignoring the quadratic and higher-order terms) can be approximated as follows (Virieux and Operto, 2009):

$$\mathbf{H} = \left[\frac{\partial \mathbf{u}^{\text{sim}}}{\partial \mathbf{m}}\right]^T \frac{\partial \mathbf{u}^{\text{sim}}}{\partial \mathbf{m}} . \tag{5}$$

FRÉCHET DERIVATIVES FOR SCATTERING-PATTERN ANALYSIS

To model the displacement $\mathbf{u}$ in heterogeneous orthorhombic media, we use the elastic wave equation:

$$\rho \frac{\partial^2 u_i}{\partial t^2} = \frac{\partial}{\partial x_j}\left[c_{ijkl}\frac{\partial u_k}{\partial x_l}\right] + F_i , \tag{6}$$

where ρ is the density, F is the body force per unit volume, and c_{ijkl} ($ijkl = 1,2,3$) are the stiffness coefficients; summation over repeated indices is implied. The solution of eq. (6) can be expressed in terms of the Green's function in the frequency domain (e.g., Kamath and Tsvankin, 2016):

$$u_n(\mathbf{x}_r, \omega) = \int_{V(\mathbf{x}')} h_i(\mathbf{x}', \omega) G_{ni}(\mathbf{x}_r, \mathbf{x}', \omega) \, dV(\mathbf{x}'), \tag{7}$$

where $h_i(\mathbf{x}', \omega)$ is the force density at location $\mathbf{x}'$, $G_{ni}(\mathbf{x}_r, \mathbf{x}', \omega)$ is the Green's function for the source at $\mathbf{x}'$ and receiver at $\mathbf{x}_r$, and the volume $V(\mathbf{x}')$ includes all sources.

Next, we obtain a general expression for the radiation patterns produced by a scatterer that represents a perturbation in one of the stiffness coefficients. To simplify the analysis, we consider the background medium to be VTI, even though the perturbation itself has orthorhombic symmetry. For instance, our model should be adequate for an orthorhombic reservoir overlaid by a VTI formation or for FWI performed with an initial VTI model. Note that most previous publications on sensitivity analysis assume the background to be purely isotropic (Pan et al., 2014; Alkhalifah and Plessix, 2014; Kamath and Tsvankin, 2016).

Following Alkhalifah and Plessix (2014) and Kamath and Tsvankin (2016), we use the Born approximation to obtain the elastic wave equation for a source that represents a perturbation in the stiffness tensor or density:

$$\tilde{\rho} \frac{\partial^2 (\delta u_i)}{\partial t^2} = \frac{\partial^2 (\delta M_{ij})}{\partial x_j} \frac{\partial}{\partial x_j} \left[\tilde{c}_{ijkl} \frac{\partial (\delta u_k)}{\partial x_l} \right] - \delta\rho \frac{\partial^2 (\tilde{u}_i)}{\partial t^2}, \tag{8}$$

where the tilde marks the unperturbed quantities, $\delta\rho$ is the density perturbation, which is equal to the difference between the densities in the perturbed (ρ) and unperturbed ($\tilde{\rho}$) media, $\delta\mathbf{u}$ is the perturbation in displacement, and $\delta M_{ij} = (\partial \tilde{u}_k / \partial x_l) \, \delta c_{ijkl}$ can be considered as the equivalent moment-tensor source that describes the stiffness perturbation $\delta c_{ijkl} = c_{ijkl} - \tilde{c}_{ijkl}$. It should be emphasized that eq. (8) takes into account the density perturbation, which is usually ignored in the literature (e.g., Pan et al., 2014, Alkhalifah and Plessix, 2014; Kamath and Tsvankin, 2016; Moradi and Innanen, 2017, 2019). Also, considering the background medium to be anisotropic makes our model more realistic.

Using eq. (7), eq. (8) can be solved in the frequency domain as:

$$\delta u_n(\mathbf{x}_r, \omega) = \int_{V(\mathbf{x}')} [(\delta\rho)\tilde{u}_i \, \omega^2 \tilde{G}_{ni}] dV(\mathbf{x}') + \int_{V(\mathbf{x}')} \left[\frac{\partial^2 (\delta M_{ij})}{\partial x'_j} \tilde{G}_{ni} \right] dV(\mathbf{x}'), \tag{9}$$

where $\tilde{G}_{ni}$ is the Green's tensor in the unperturbed (background) medium due to the scattering source at location $\mathbf{x}'$. Integration by parts in the far-field approximation yields the scattered wavefield:

$$\delta u_n(\mathbf{x}_r, \omega) \approx \int_{V(\mathbf{x}')}\left[(\delta F_i)\tilde{G}_{ni}\right]dV(\mathbf{x}') - \int_{V(\mathbf{x}')}\left[(\delta M_{ij})\tilde{G}_{ni,j}\right]dV(\mathbf{x}'), \qquad (10)$$

where $\delta F_i = (\delta\rho)\tilde{u}_i\,\omega^2$, and $\tilde{G}_{ni,j} = \partial^2\tilde{G}_{ni}/\partial x_j'$. By taking the partial derivatives of the scattered wavefield with respect to the variations of the model parameters (m_k), we find the Fréchet derivatives for a general anisotropic medium:

$$\frac{\partial[\delta u_n(\mathbf{x}_r,\omega)]}{\partial m_k} \approx \int_{V(\mathbf{x}')}\left\{\left[\frac{\partial(\delta F_i)}{\partial m_k}\right]\tilde{G}_{ni} - \left[\frac{\partial(\delta M_{ij})}{\partial m_k}\right]\tilde{G}_{ni,j}\right\}dV(\mathbf{x}'). \qquad (11)$$

Note that the Fréchet derivatives are widely used for model updating in linearized inversion algorithms, such as reflection tomography (e.g., Wang and Tsvankin, 2013a,b). Computation of the inversion gradient in FWI, however, is typically based on the more efficient adjoint-state method.

SCATTERING PATTERNS AND EFFECTIVE MOMENT TENSOR

Scattering (radiation) patterns have been used to evaluate the sensitivity of FWI to the parameters of anisotropic media (Gholami et al., 2013; Operto et al., 2013; Alkhalifah and Plessix, 2014; Kamath and Tsvankin, 2016). Most existing results, however, are limited to transversely isotropic (often acoustic) models and/or assume the background to be isotropic. Here, we use the Fréchet derivatives [eq. (11)] to study the radiation patterns for an elastic orthorhombic scatterer embedded in a VTI background (Singh and Tsvankin, 2020).

An orthorhombic medium with fixed orientations of the symmetry planes is described by nine stiffness coefficients and density (Fig. 1). Henceforth, we assume that the symmetry planes coincide with the Cartesian coordinate planes. The equivalence between the symmetry planes of orthorhombic and TI media allowed Tsvankin (1997, 2012) to replace the stiffnesses with the following notation:

V_{P0}: the P-wave vertical velocity;
V_{S0}: the velocity of the vertically traveling S-wave polarized in the x_1-direction;
$\varepsilon^{(1)}$, $\delta^{(1)}$, and $\gamma^{(1)}$: the VTI parameters in the $[x_2, x_3]$-plane (the superscript indicates the axis perpendicular to the corresponding plane);

is a similarly defined parameter that absorbs the influence of the coefficient $\delta^{(3)}$, V_{S1} is the vertical velocity of the S-wave polarized in the x_2-direction, and V_{S2} is the horizontal velocity of the SH-waves in both vertical symmetry planes. Note that the SH-waves in the vertical symmetry planes represent two different shear modes (e.g., the fast wave S_1 in the $[x_1, x_3]$-plane and slow wave S_2 in the $[x_2, x_3]$-plane), as discussed by Tsvankin (1997, 2012). Kamath et al. (2017) discuss the advantages of a similar parameterization in reducing the trade-offs for VTI media.

Following Kazei and Alkhalifah (2019), we substitute a plane wave into eq. (11). Then the total displacement field due to the perturbations in both the density and stiffness coefficients can be concisely obtained for an arbitrarily anisotropic background medium as:

$$\delta \mathbf{u}(\mathbf{x}_r, \omega) = \mathcal{B}[\mathbf{S}(\delta \mathbf{F}) + \mathbf{S}(\delta \mathbf{M})\mathbf{D}], \tag{15}$$

where the vector $\mathcal{B}$ incorporates the components of the Green's tensors [see Shaw and Sen (2004), and Pan et al. (2014), for details], the term in the brackets is defined as the radiation (or scattering) pattern, and $\delta \mathbf{F}$ is the virtual force due to the density perturbation: $\delta \mathbf{F} = (\delta \rho)\mathbf{I}$. The vectors $\mathbf{I}$ and $\mathbf{S}$ correspond to the incident and scattered waves, respectively, and are defined as $\mathbf{R}$ (for P-waves), $\mathbf{\Theta}$ (for SV-waves), or $\mathbf{\Phi}$ (for SH-waves) depending on the incident and scattered wave type:

$$\mathbf{R} = \begin{bmatrix} \sin\theta\cos\emptyset \\ \sin\theta\sin\emptyset \\ \cos\theta \end{bmatrix}, \qquad \mathbf{\Theta} = \begin{bmatrix} \cos\theta\cos\emptyset \\ \cos\theta\sin\emptyset \\ -\sin\theta \end{bmatrix}, \qquad \mathbf{\Phi} = \begin{bmatrix} -\sin\emptyset \\ \cos\emptyset \\ 0 \end{bmatrix},$$

where θ is the incidence angle measured counter-clockwise from the x_3-axis and $\emptyset$ is the azimuth measured counter-clockwise from the x_1-axis. For example, for the PSV-wave the incident mode is P and the scattered one is SV, so $\mathbf{I} = \mathbf{R}$ and $\mathbf{S} = \mathbf{\Theta}$. The vector $\mathbf{D}$ in eq. (15) is equal to $\mathbf{R}$, whereas $\delta \mathbf{M}$ represents the effective moment tensor that describes the stiffness perturbations:

$$\delta M_{ij} = \begin{bmatrix} \delta c_{11}e_{11} + \delta c_{12}e_{22} + \delta c_{13}e_{33} & 2 + \delta c_{66}e_{12} & 2 + \delta c_{55}e_{13} \\ 2 + \delta c_{66}e_{12} & \delta c_{12}e_{11} + \delta c_{22}e_{22} + \delta c_{23}e_{33} & 2 + \delta c_{44}e_{13} \\ 2 + \delta c_{55}e_{13} & 2 + \delta c_{44}e_{13} & \delta c_{13}e_{11} + \delta c_{23}e_{22} + \delta c_{33}e_{33} \end{bmatrix}, \tag{16}$$

where e_{ii} is the strain tensor. The exact tensors $\delta \mathbf{M}$ for the velocity-based parameterization employed here are listed in the Appendix. Note that because $\delta \mathbf{M}$ depends on the stiffnesses, in our notation it represents a function of the velocities and density.

Computation of radiation patterns

The acquisition geometry used to examine the radiation patterns is shown in Fig. 2. The patterns are computed for five different azimuths of the source-receiver line. The so-called "opening angles" between the incident and scattered waves vary (see below) from 0° to 360° to account for both reflected and transmitted modes.
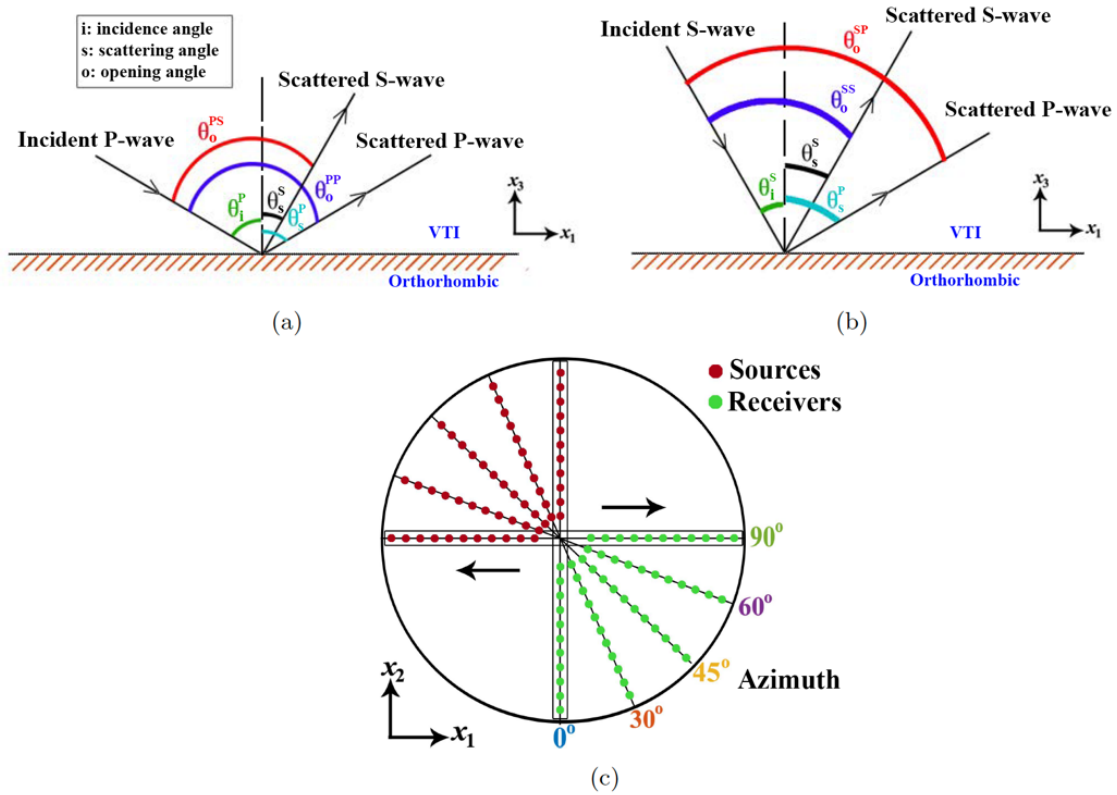

Fig. 2. Acquisition geometry for radiation pattern analysis: (a) and (b) the $[x_1, x_3]$- plane, and (c) the $[x_1, x_2]$- plane. The sources and receivers are distributed along five constant-azimuth lines with the opening angles ranging from 0° to 360°. The vertical symmetry planes correspond to azimuths of 0° and 90°, and arrows point toward the increase in the opening angle. The parameters of the background VTI medium are: V_{P0} = 2.0 km/s, V_{S0} = 1.43 km/s, $\varepsilon \approx 0.28$, $\delta \approx 0.05$, $\gamma \approx 0.09$, and ρ = 2.2 g/cm^3. For typical values of the VTI parameters the radiation patterns are not strongly dependent on the background properties (see below). However, the critical angles for the S-to-P conversions depend on the V_{S0}/V_{P0} −ratio and the coefficients ε and δ.

The phase angles made by the incident (θ_i) and scattered (θ_s) waves with the vertical satisfy Snell's law:

$$\frac{\sin\theta_i}{V_i(\theta_i)} = \frac{\sin\theta_s}{V_s(\theta_s)}, \tag{17}$$

where V_i and V_s are the phase velocities of the incident and scattered waves, respectively.

The exact phase velocities of P- and SV-waves in VTI media are given by (e.g., Tsvankin, 2012):

$$2\rho V^2(\theta) = (c_{11} + c_{55})\sin^2\theta + (c_{33} + c_{55})\cos^2\theta \pm \sqrt{[(c_{11} - c_{55})\sin^2\theta - (c_{33} - c_{55})\cos^2\theta]^2 + 4(c_{13} + c_{55})\sin^2\theta\cos^2\theta}, \tag{18}$$

where the plus sign in front of the radical corresponds to the P-wave, and the minus to the SV-wave. The SH-wave phase velocity can be found as:

$$V_{SH}(\theta) = \sqrt{\frac{c_{66}\sin^2\theta + c_{55}\cos^2\theta}{\rho}}, \tag{19}$$

If the incident and scattered modes are of the same type (e.g., PP or SVSV), their velocities are equal ($V_i = V_s$), and the incidence and scattering angles coincide ($\theta_i = \theta_s$). Then the opening angle (θ_0) between the incident and scattered rays is twice the incidence angle. For instance, the opening angle for PP-waves $\theta_0^{PP} = 2\theta_i^{P}$.

The scattering and incidence angles are different for mode-converted waves (e.g., PS). After obtaining the scattering angle θ_s using eq. (18) [or eq. (19) for the SH-wave], we can find the opening angle for the PS-wave (PSV or PSH) as $\theta_0^{PS} = \theta_i^{P} + \theta_s^{S}$. The opening angles for the SVP and SHP conversions are obtained in the same way.

For S-to-P conversions, the incidence angle in our analysis is limited by the critical angle, for which the scattered P-wave travels horizontally. At postcritical S-wave incidence, the P-wave becomes inhomogeneous (evanescent) and its amplitude exponentially decays away from the scatterer.

The opening angles for the SVSH or SHSV conversions are obtained in the same way as those for PS-waves. Depending on the relationship between the SH- and SV-wave velocities, it may be possible to encounter the critical angles for the SVSH- or SHSV-waves. However, the scattering

amplitudes for these modes are relatively small and the conversions between the S-waves are not included in the discussion below.

The radiation patterns are computed as functions of the opening phase angles that can be recalculated into the corresponding group (ray) angles using the well-known group-velocity equations (e.g., Tsvankin, 2012). Note that the relationship between group and phase angles depends on the parameters of the VTI background medium.

ANALYSIS OF RADIATION PATTERNS

Overlap of the radiation patterns for different parameters indicates possible trade-offs that would hinder parameter updates and reduce the accuracy and resolution of the inversion results. First, we evaluate the influence of the scattering angles and the frequency range on the model updates.

The scattering wavenumber vector ($\mathbf{k}$) depends on the opening angle θ and angular frequency ω (Virieux and Operto, 2009):

$$\mathbf{k} = \frac{\omega}{\vartheta}\cos\frac{\theta_0}{2}\,\boldsymbol{n}\,,\tag{20}$$

where ϑ is the medium velocity and $\boldsymbol{n}$ is the unit vector normal to the reflector. In a multiscale inversion designed to improve the convergence of FWI, lower frequencies are used first in model updating. The obtained inversion results are used to build the initial model for the next (higher) frequency range, etc. Restricting the input data to low frequencies and relatively large opening angles θ_0 (long offsets) helps generate low-wavenumber (long-wavelength) updates and reduce the nonlinearity of the inversion.

Here, we analyze the radiation patterns for different parameter perturbations to gain insight into the corresponding updates and potential parameter trade-offs. The effective moment tensors for the perturbations of the P-wave horizontal velocities V_{P1} and V_{P2} are given in eqs. (A-3) and (A-4), respectively. Figs. 3-7a, b indicate that the low-wavenumber models of V_{P1} and V_{P2} can be reconstructed only if data at uncommonly large opening angles are available [eq. (20)]. Even for long-offset surveys, such wide opening angles can be achieved only in the shallow part of the model. The radiation patterns for the velocities V_{P1} and V_{P2} are well separated for all modes with the exception of the pure SH-waves, where there is a significant overlap (Figs. 7b, c).

A perturbation in the P-wave vertical velocity V_{P0} produces an intensive scattered PP-wave for narrow opening angles (Fig. 3a). Because the wavenumber is proportional to the cosine of the opening angle [eq. (20)], we can expect to obtain high-wavenumber updates in V_{P0} from conventional-spread PP reflection data (Fig. 3a). The converted PSV-waves should yield lower-wavenumber updates in V_{P0} because the maximum of their radiation pattern corresponds to intermediate opening angles (Fig. 4a). Because the background medium is VTI and a perturbation of the velocity V_{P0} is represented by a virtual explosive source [eq. (A-2)], the scattered SV-wave amplitudes are generally smaller than those of P-waves (Fig. 6a), whereas SH-waves should not be excited at all (Tsvankin, 2012).
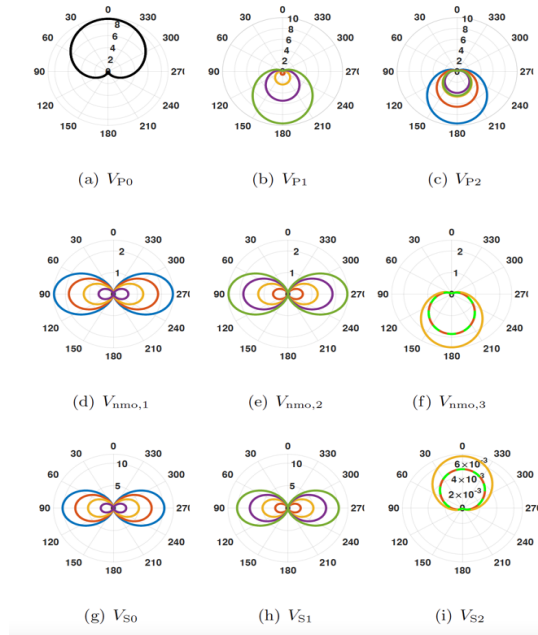

Fig. 3. Radiation patterns of the pure PP-waves computed as a function of the opening angle (shown along the perimeter). The colors correspond to the azimuths of the source-receiver lines shown in Fig. 2: $\emptyset = [0^0, 30^0, 45^0, 60^0, 90^0]$. The radiation pattern on plot (a) is azimuthally invariant. The dashed (green-red) lines on plot (g) mark the identical patterns corresponding to azimuths of 30^0 and 60^0.

The effective moment-tensor sources that represent perturbations in the shear-wave vertical velocities V_{S0} and V_{S1} [eqs. (A-8) and (A-9)] radiate most energy in the vertical plane that includes the source and receiver. Figs.3-5 [g, h] suggest that if PP reflections or PSV/PSH conversions are acquired at intermediate opening angles, the parameters V_{S0} and V_{S1} can be estimated for a range of intermediate wavenumbers. Low-wavenumber model updates in V_{S0} and V_{S1} can be obtained from the pure SV- and SH-waves at narrow opening angles (Figs. 6-7 [g, h]). The patterns of these two parameters are well separated for all wave types (except for the PSH-waves) and azimuths. In contrast, the patterns of the PP, PSH, and SVSV reflections

due to the perturbations of V_{S0} and V_{S1} have a significant overlap with the corresponding patterns of $V_{nmo,1}$ and $V_{nmo,2}$ (Figs. 3,5,6[d-e]-[g-h]). The scattering amplitudes for V_{S0} and V_{S1}, however, are much larger than those for $V_{nmo,1}$ and $V_{nmo,2}$. Therefore, errors in the S-wave vertical velocities should degrade the updates of the NMO velocities, but less so the other way around. The trade-offs between the S-wave vertical velocities and the P-wave NMO velocities can be mitigated by including the PSV conversions and/or pure SV- and SH-waves.
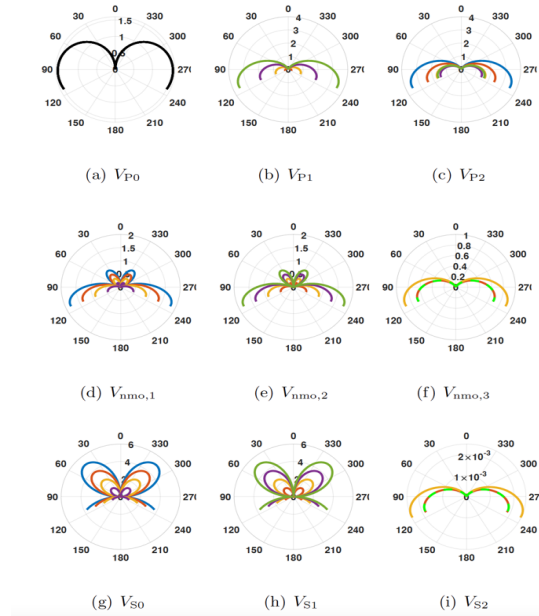

Fig. 4. Radiation patterns of the PSV-waves.

Reliable estimation of the S-wave horizontal velocity V_{S2} requires acquisition of the pure SH-waves which are polarized horizontally in the VTI background (Fig. 7i). This conclusion agrees with the results of Oh and Alkhalifah (2019). The parameter $V_{nmo,3}$ potentially can be updated using all wave types at wide opening angles and intermediate azimuths (Figs. 3-7f). However, estimation of $V_{nmo,3}$ from field data could be challenging because it requires high-quality wide-azimuth data recorded for large scattering angles (i.e., long offsets).

Fig. 8 shows that the pure P-waves are more sensitive to density than the other modes and could be used for updating the high-wavenumber density model. The intermediate-wavenumber density field can also be reconstructed from PSV-waves acquired at intermediate opening angles. Although the contributions of the pure SV- and SH-waves to density inversion are expected to be smaller than those of the pure P-waves, these modes can potentially help in updating density with both low and high wavenumbers.
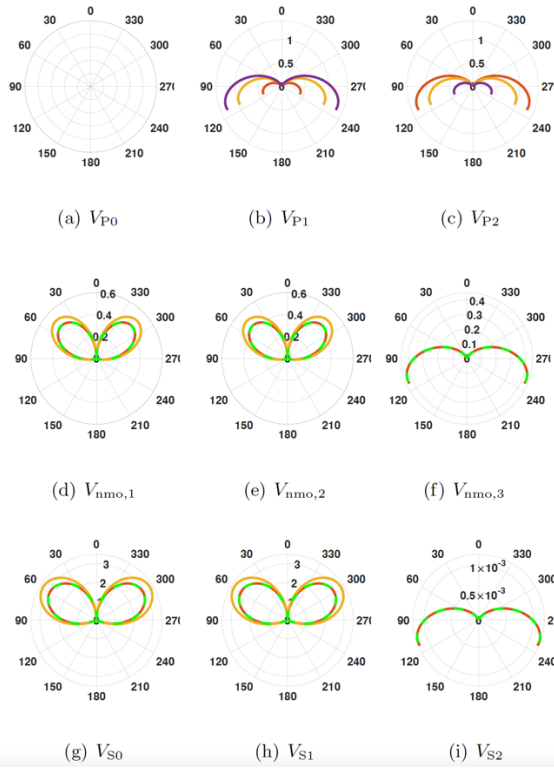
Fig. 5. Radiation patterns of the PSH-waves, which are generated only outside the vertical symmetry planes of the orthorhombic medium.
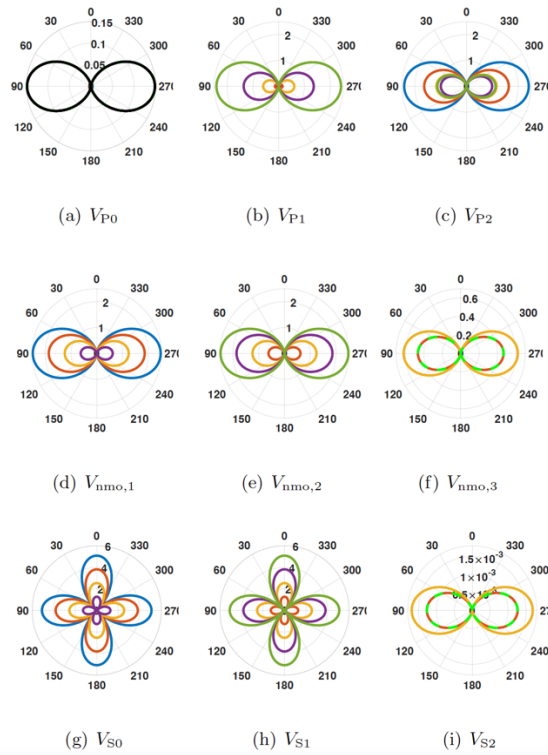

Fig. 6. Radiation patterns of the pure SV-waves.

(a) V_{P0} (b) V_{P1} (c) V_{P2}

(d) $V_{nmo,1}$ (e) $V_{nmo,2}$ (f) $V_{nmo,3}$

(g) V_{S0} (h) V_{S1} (i) V_{S2}
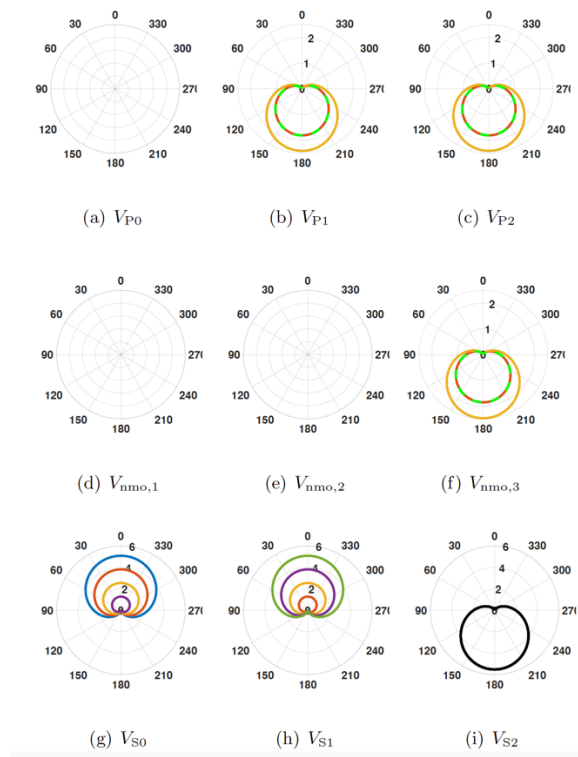
Fig. 7. Radiation patterns of the pure SH-waves.

(a) PP   (b) SVSV   (c) SHSH   (d) PSV

(e) SVP   (f) PSH   (g) SHP
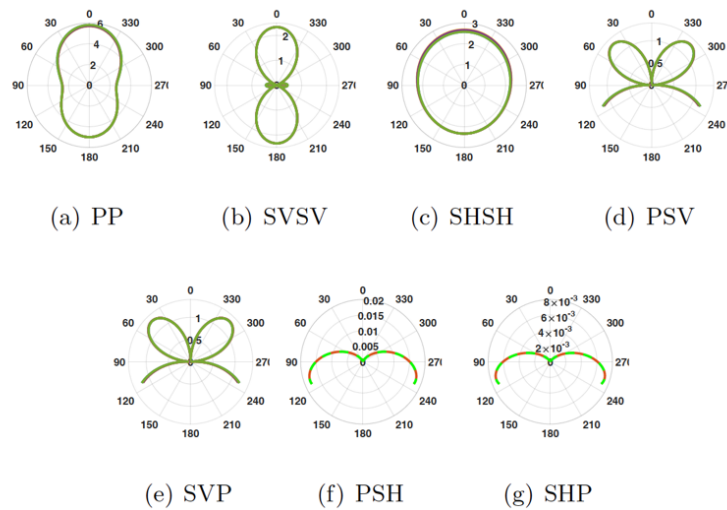
Fig. 8. Radiation patterns corresponding to the density perturbation. For a wide range of background anisotropy parameters, these patterns are found to be azimuthally invariant.

It should be emphasized that the radiation patterns discussed above are computed for a homogeneous VTI overburden above an orthorhombic layer (perturbation) and do not account for attenuation. However, despite the

simplicity of this model, these patterns still provide important insights into parameter trade-offs and possible model-updating strategies for more realistic subsurface structures.

Dependence of radiation patterns on background medium

The radiation patterns discussed above are generated for a homogeneous VTI background medium with the following parameters: $V_{P0} = 2.0$ km/s, $V_{S0} = 1.43$ km/s, $\varepsilon \approx 0.28$, $\delta \approx 0.05$, $\gamma \approx 0.09$, and $\rho = 2.2$ g/cm^3. Whereas these values fall within the typical range for such sedimentary rocks as shales, it is important to evaluate the influence of the background anisotropy on the radiation patterns.

Below we discuss the radiation patterns of both pure and converted modes for the Thomsen background coefficients ε, γ, and δ varying within the most plausible range (between 0 and 0.4 for ε and γ, and between -0.1 and 0.3 for δ). It should be emphasized that, even though the shape of the radiation patterns for all parameters remains almost unchanged within these ranges of ε, δ, and γ, the amplitude of the patterns exhibits some dependence on the background anisotropy, and these changes vary with azimuth.

Radiation patterns of pure modes (PP, SVSV, and SHSH)

As discussed above, if the incident and scattered modes are of the same type, the opening angle (θ_0) is twice the incidence angle, irrespective of the background medium. However, the corresponding moment tensors [eqs. (A-2)-(A-11)] depend on the background parameters, which could change the corresponding radiation patterns.

The pure-mode radiation patterns for the P-wave vertical velocity V_{P0} [eq. (A-2)] are insensitive to ε and γ. Furthermore, the radiation patterns of the PP- and SHSH-waves are practically independent of δ. However, the scattered amplitude of the SVSV-wave for a perturbation in V_{P0} increases by up to 30% when δ changes from -0.1 to 0.3. For the P-wave horizontal velocity V_{P1}, the pure-mode radiation patterns [eq. (A-3)] are independent of δ and γ, but their amplitude varies (by up to 35%) with ε. Whereas the patterns for the P-wave NMO velocities $V_{\mathrm{nmo},1}$ and $V_{\mathrm{nmo},2}$ [eqs. (A-5) - (A-6)] are not sensitive to ε and γ, the scattering amplitudes get larger with increasing δ. The radiation patterns for the S-wave vertical velocities V_{S0} and V_{S1} are practically independent of the background anisotropy coefficients.

The radiation patterns for density depend on all three background Thomsen coefficients [eq. (A-11)]. The scattering amplitudes for a perturbation in density generally increase for relatively large positive values of ε, δ, and γ.

Radiation patterns of converted PSV- and PSH-waves

For converted modes, the opening angle (θ_0) should be computed from eqs. (17)-(19), which include the background parameters. Note that the critical angles in this case also vary with the background vertical velocities and anisotropy coefficients.

For a perturbation in V_{P0}, the PSV-wave amplitude changes by up to 35% for δ within the range [-0.1, 0.3]. In contrast, δ has a weak influence on the PSH-wave scattered by a V_{P0}-perturbation. The converted-wave radiation patterns for V_{P1} change by up to 35% with ε varying from 0 to 0.4.

The PSV- and PSH-wave radiation patterns for the other parameters of orthorhombic media have a similar dependence on the background medium as the corresponding patterns for the pure modes.

EXAMPLE OF FWI FOR LAYERED ORTHORHOMBIC MEDIA

To verify the above results, we perform elastic FWI for a horizontally layered orthorhombic/VTI model, which generally conforms to the assumptions behind the radiation-pattern analysis. The elastic wave eq. (6) is solved using fourth-order finite-differences (Albertin et al., 2016) on a staggered grid with CPML (convolutional perfectly matched layers) boundary conditions on the sides and bottom of the model and a free surface on top. A more detailed description of the FWI algorithm can be found in a companion paper (Singh et al., 2021). As before, the medium is parameterized by the vertical velocities V_{P0} and V_{S0}, density, and the velocities defined in eqs. (12)-(14).

The model includes two horizontal orthorhombic layers embedded in a VTI background medium. The velocities from eqs. (12)-(14) are obtained by scaling the fields of V_{P0} and V_{S0}. To simulate marine data, the section is overlaid by a 260 m-thick water layer (Fig. 10 a-j). We generate the displacement field that could be acquired on the sea floor. The wavefield is excited by 100 shots and recorded by 1296 receivers placed 40 m and 260 m, respectively, beneath the free surface and evenly distributed over the horizontal plane. The source represents a point explosion and produces a Ricker wavelet with a central frequency of 10 Hz.

Frequencies below 2 Hz are assumed to be unavailable, which is usually the case in practice. To mitigate inversion nonlinearity, a multiscale FWI approach is employed in two frequency bands (2-10 Hz and 2-20 Hz). The inversion gradients [eq. (4)] are preconditioned following the scheme described by Plessix and Mulder (2004), which is designed to compensate for amplitude loss due to geometric spreading.
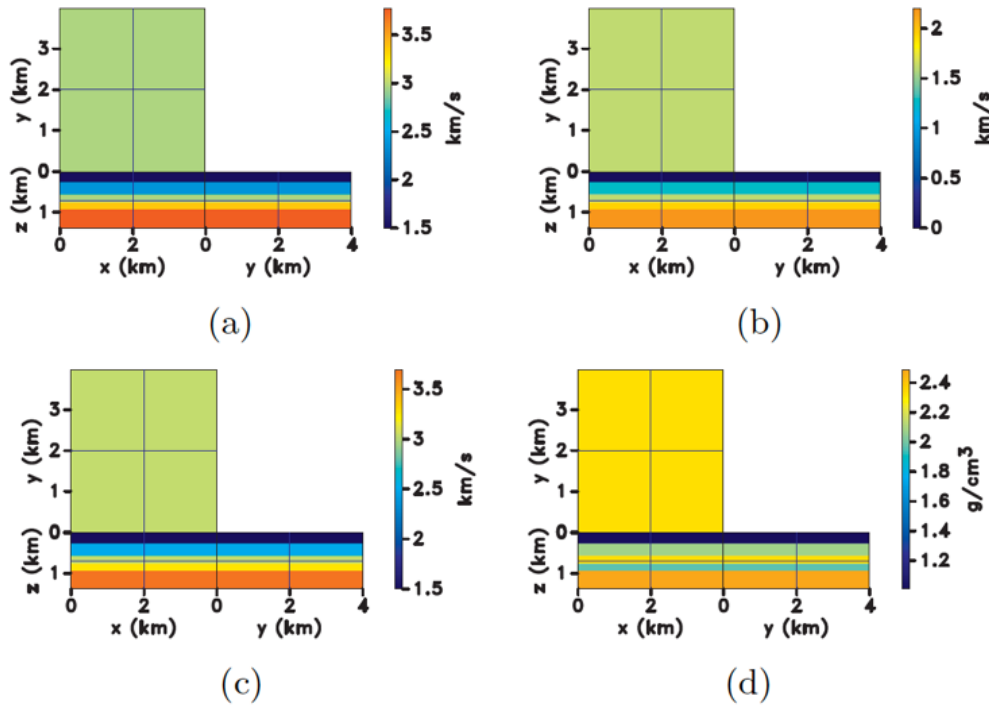
Fig. 10. Parameters of the layered model used in the FWI test: (a) the P-wave vertical velocity (V_{P0}), (b) the S-wave vertical velocity (V_{S0}), (c) the P-wave NMO velocity in the $[x_2, x_3]$-plane ($V_{\mathrm{nmo},1}$), and (d) the density (ρ). The cross-sections correspond to the symmetry planes of the orthorhombic layers which coincide with the Cartesian coordinate planes.

The initial model for FWI is obtained by smoothing the actual parameter distributions. Typically, such long-wavelength velocity models are built using reflection tomography or moveout inversion (Tsvankin and Grechka, 2011; Wang and Tsvankin, 2013a,b; Ivanov and Stovas, 2017; Liu and Tsvankin, 2019).

The radiation patterns discussed in the previous section represent the magnitude of the displacement field from a certain parameter perturbation. Because FWI typically operates with displacement components, here we verify the results of the sensitivity analysis by inverting just the vertical displacement.

Fig. 11 displays vertical parameter profiles that illustrate the accuracy of the initial model and the inversion results. The inverted parameters V_{P0}, V_{S0}, $V_{\mathrm{nmo},1}$, and ρ are shown in Fig. 12. The accuracy of the updates in V_{P0} and V_{S0} is illustrated in Fig. 13. Although the algorithm reduces the objective function by 90%, the P-wave NMO velocities are not well resolved.
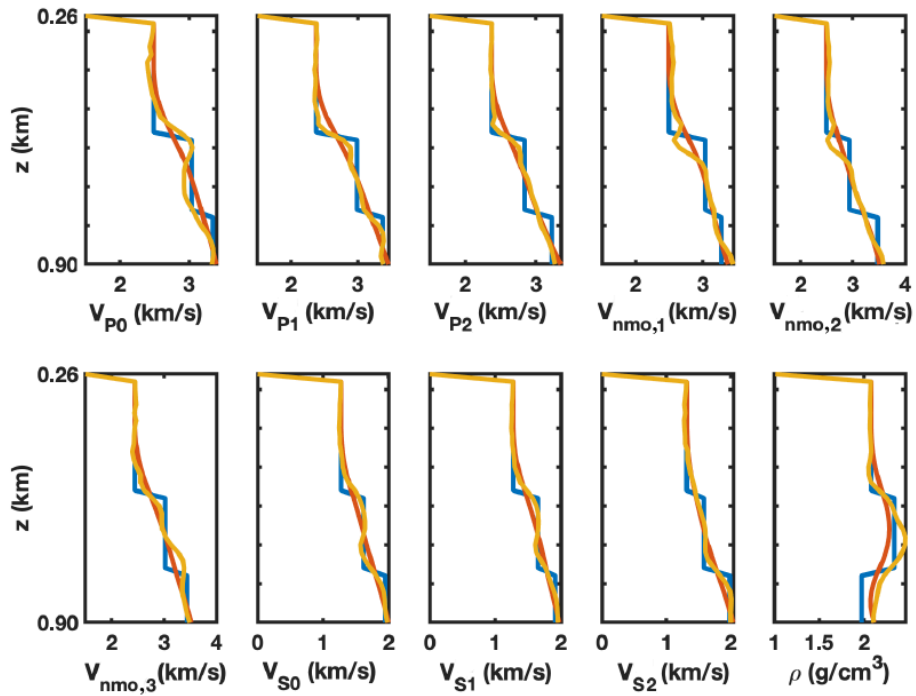
Fig. 11. Vertical parameter profiles at $x = y = 110$ km. The actual, initial, and inverted parameters are marked by the blue, red, and yellow lines, respectively.
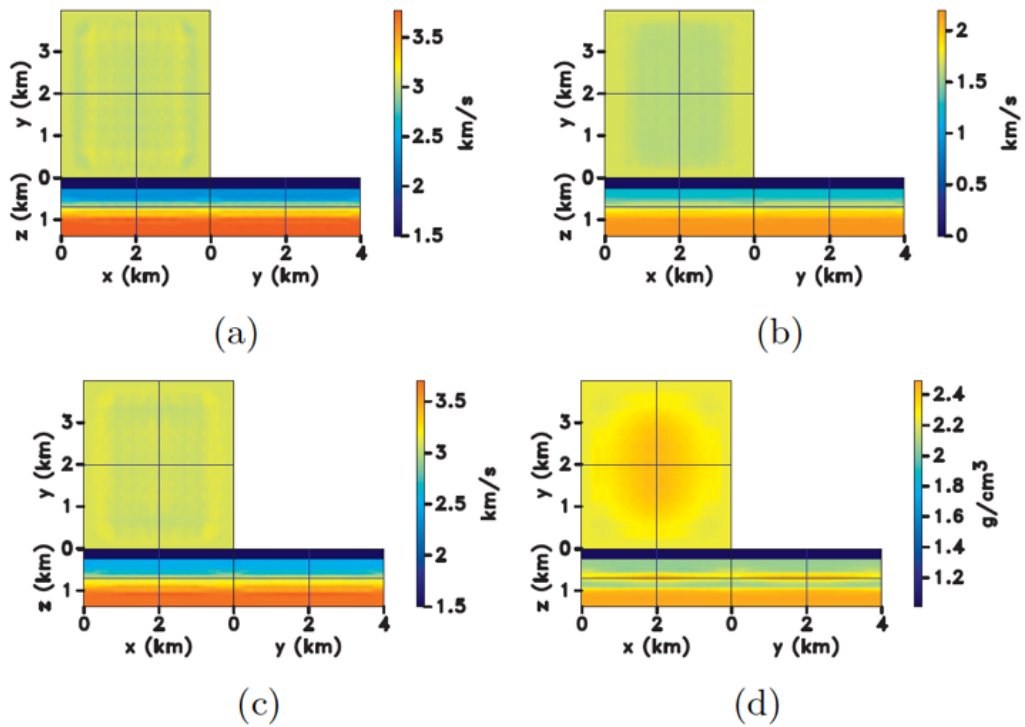

Fig. 12. Inverted parameters: (a) V_{P0}, (b) V_{S0}, (c) $V_{nmo,1}$, and (d) ρ.
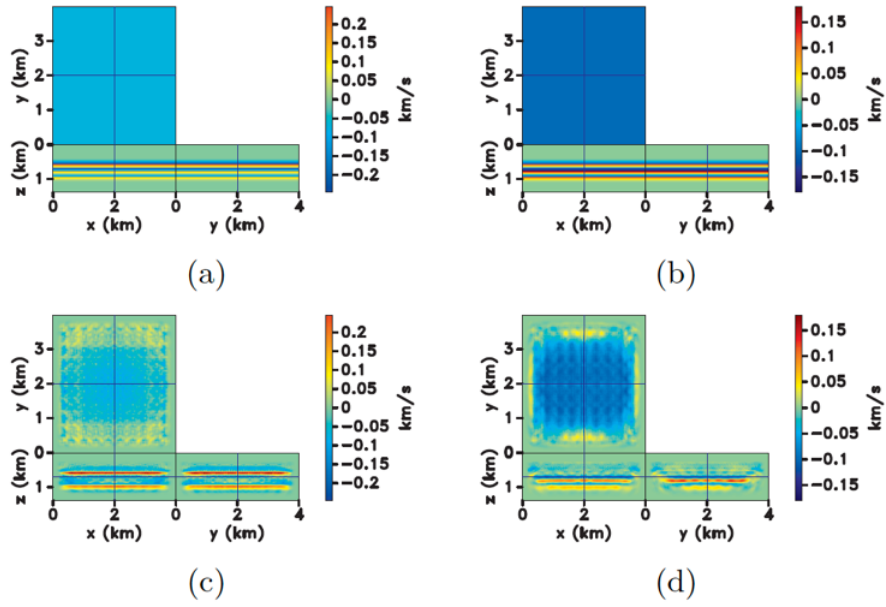
Fig. 13. Difference between the actual parameters (a) V_{P0} and (b) V_{S0} and their initial values. The difference between the parameters (c) V_{P0} and (d) V_{S0} estimated by FWI and their initial values.

The P-wave horizontal velocities (V_{P1} and V_{P2}) are accurately estimated in the top orthorhombic layer but they are barely updated in the second layer. This is supported by the sensitivity analysis (Figs. 3b,c), which shows that low-wavenumber updates in V_{P1} and V_{P2} require large opening angles. For the offset range in our synthetic data set, such angles can be reached only for reflections from the bottom of the shallow layer. Because of the well-separated radiation patterns of the P-wave horizontal velocities (Fig. 3-6b, c), the trade-offs between V_{P1} and V_{P2} are insignificant. Due to the high sensitivity of the pure-mode P data to the P-wave vertical velocity (Fig. 3a), the inverted V_{P0} closely matches the actual values for both orthorhombic layers.

The radiation patterns in Figs. 3-5g,h indicate that the pure P-waves and converted PSV and PSH reflections make the largest contributions to intermediate-wavenumber updates in the S-wave vertical velocities V_{S0} and V_{S1}. The pure SV-waves (Figs. 6g,h) are sensitive to these parameters at both narrow and wide opening angles, which helps update the small- and large-wavenumber components of V_{S0} and V_{S1}.

Note that explosive sources used in this test do not produce the horizontally polarized SH-waves in the VTI overburden, which are needed to update the S-wave horizontal velocity V_{S2} (Fig. 7i). However, P-waves incident on the top of the orthorhombic medium outside the vertical symmetry planes generate P-to-SH conversions. These PSH reflections and

their multiples in the overburden help estimate V_{S2} in a segment of the top orthorhombic layer.

The radiation patterns also reveal significant trade-offs (Figs. 3,5,6 [d, e, g, h]) between the P-wave NMO velocities $V_{nmo,1}$ and $V_{nmo,2}$ and the S-wave velocities V_{S0} and V_{S1}. These trade-offs could explain the wrong sign of the updates in the NMO velocities near the top of the first orthorhombic layer. In general, the updates in $V_{nmo,1}$ and $V_{nmo,2}$ are small, which is in agreement with the relatively low magnitudes of their radiation patterns. Because FWI is weakly sensitive to the velocity $V_{nmo,3}$ (Fig. 3f), that parameter is poorly resolved and stays close to its initial values, even though the input data include relatively wide opening angles (the maximum opening angles for the first and second orthorhombic layers are about 144° and 130°, respectively).

The density, which is often difficult to constrain from surface seismic data, can be accurately recovered down to the middle of the first orthorhombic layer (where it is overestimated). Beneath that depth, FWI fails to produce tangible updates in ρ. The sensitivity analysis (Fig. 8) shows that the high-wavenumber density model can be updated using narrow-angle (small-offset) PP reflections. Because the recorded amplitudes decrease with reflector depth, the upper part of the model is better illuminated by the reflected PP data. The radiation patterns also indicate that the resolution of the density model could be improved using the pure SV and SH reflections, whose amplitudes in this test are insignificant.

It should be noted that sensitivity analysis is an approximate tool based on a relatively simple perturbation model, whose results cannot be exactly verified by performing actual FWI. In particular, the output of FWI may change depending on the employed objective function, gradient preconditioning, initial model, specific application of the multiscaling method, etc.

CONCLUSIONS

We implemented a formalism to compute the radiation (sensitivity) patterns for an orthorhombic perturbation overlaid by a homogeneous VTI medium. The perturbations in the velocities and density are described by the moment tensor of the effective source responsible for the scattered wavefield. In addition, the density perturbation is represented by a frequency-dependent effective force. Sensitivity analysis was performed using a convenient velocity-based parameterization that incorporates Tsvankin's anisotropy coefficients.

The pure P-wave radiation patterns for different parameters show the least overlap compared to the other modes, which indicates fewest parameter

trade-offs. In particular, acquisition of the PP reflections for a wide range of opening angles helps resolve the P-wave velocities along the symmetry directions of orthorhombic media (V_{P0}, V_{P1}, and V_{P2}). The S-wave vertical velocities (V_{S0} and V_{S1}) can also be estimated from the pure P-waves for a range of intermediate wavenumbers, although their recovery is somewhat hindered by trade-offs with the P-wave NMO velocities. The mode-converted PSV-waves can contribute to the intermediate-wavenumber updates of the P- and S-wave symmetry-direction velocities V_{P1}, V_{P2}, V_{S0}, and V_{S1}.

The magnitudes of the radiation patterns of the PSH- and pure SV-waves are too small for these modes to have a significant impact on FWI, with the possible exception of updating the S-wave vertical velocities. Also, there are trade-offs between V_{S0} and V_{S1} and the P-wave NMO velocities $V_{\mathrm{nmo,1}}$ and $V_{\mathrm{nmo,2}}$, for the PP, PSV, PSH, and SVSV reflections. These trade-offs mostly degrade the estimates of the velocities $V_{\mathrm{nmo,1}}$ and $V_{\mathrm{nmo,2}}$, which produce low-amplitude radiation patterns. One option to increase the accuracy of $V_{\mathrm{nmo,1}}$ and $V_{\mathrm{nmo,2}}$ is to include the pure SH reflections in the inversion. If the SH-waves are acquired at wide opening angles, they also can help resolve the low-wavenumber components of the shear-wave horizontal velocity V_{S2}. Constraining the parameter $V_{\mathrm{nmo,3}}$ requires acquisition of high-quality wide-azimuth, long-offset data, which may be problematic in practice.

The PP reflections can be used to reconstruct the high-wavenumber component of the density field, whereas the PSV data provide information for intermediate-wavenumber density updating. Acquisition of SV-to-P and SH-to-P conversions may not be justified for FWI purposes because their scattered amplitudes are small, and they are not expected to mitigate parameter trade-offs.

We also discussed the influence of the background VTI parameters on the radiation patterns of the pure and converted waves and demonstrated that the background anisotropy should be taken into account in sensitivity analysis and, therefore, in FWI. The conclusions drawn from evaluating the radiation patterns are in broad agreement with FWI results for a model composed of two horizontal orthorhombic layers beneath a VTI medium. Further confirmation of our results is provided by Singh et al. (2021), who present synthetic tests for realistic orthorhombic models.

REFERENCES

Albertin, U., Shen, P., Sekar, A., Johnsen, T., Wu, C., Nihei, K. and Bube, K., 2016. 3D orthorhombic elastic full-waveform inversion in the reflection domain from hydrophone data. Expanded Abstr., 86th Ann. Internat. SEG Mtg., Dallas: 1094-1098.

Alkhalifah, T. and Plessix, R.-E., 2014 A recipe for practical full-waveform inversion in anisotropic media: An analytical parameter resolution study. Geophysics, 79(3): R91-R101.

Bakulin, A., Grechka, V. and Tsvankin, I., 2000a. Estimation of fracture parameters from reflection seismic data – Part I: HTI model due to a single fracture set. Geophysics, 65: 1788-1802.

Bakulin, A., Grechka, V. and Tsvankin, I., 2000b. Estimation of fracture parameters from reflection seismic data – Part II: Fractured models with orthorhombic symmetry. Geophysics, 65: 1803-1817.

Duan, Y. and Sava, P., 2015. Scalar imaging condition for elastic reverse time migration. Geophysics, 80(4): S127-S136.

Gholami, Y. Brossier, R., Operto, S., Ribodetti, A. and Virieux, J., 2013. Which parametrization for acoustic VTI full waveform inversion? Part 1: Sensitivity and trade-off analysis. Geophysics, 78(2): R81-R105.

Grechka, V. and Tsvankin, I., 1999. 3-D moveout velocity analysis and parameter estimation for orthorhombic media. Geophysics, 64: 820-837.

Grechka, V. and Tsvankin, I., 2002. NMO-velocity surfaces and Dix-type formulas in anisotropic heterogeneous media. Geophysics, 67: 939-951.

Hale D., 2010. Image-guided 3D interpolation of borehole data. Expanded Abstr., 80th Ann. Internat. SEG Mtg., Denver: 1266-1270.

Ibanez-Jacome, W., Alkhalifah, T. and Waheed, U.B., 2014. Effective orthorhombic anisotropic models for wavefield extrapolation. Geophys. J. Internat., 198: 1653-1661.

Ivanov, Y. and Stovas, A., 2017. Traveltime parameters in tilted orthorhombic media. Geophysics, 82(6): C187-C200.

Kazei, V. and Alkhalifah, T., 2019. Scattering radiation pattern atlas: what anisotropic elastic properties can body waves resolve? J. Geophys. Res., 124: 2781-2811.

Kamath, N. and Tsvankin, I., 2016. Elastic full-waveform inversion for VTI media: Methodology and sensitivity analysis. Geophysics, 81(2): C53-C68.

Kamath, N., Tsvankin, I. and Diaz, E., 2017. Elastic full-waveform inversion for VTI media: A synthetic parameterization study. Geophysics, 82(5): C163-C174.

Liu, Q. and Tsvankin, I., 2019. Stacking-velocity tomography for tilted orthorhombic media. Geophysics, 84(3): C171-C180.

Liu, Q. and Tromp, J., 2006. Finite frequency kernels based on adjoint methods. Bull. Seismol. Soc. Am., 96: 2383-2397.

Li, Y., Han, W., Chen, C.-S. and Huang, T., 2012. Velocity model building for tilted orthorhombic depth imaging. Expanded Abstr., 82nd Ann. Internat. SEG Mtg., Las Vegas: 1-5.

Maitra, S., Basir, F.F., Ghazali, M.L., Ghazali, A.R., Sapiai, S.M., El-K., N. and Konuk, T., 2018. Orthorhombic full-waveform inversion and model building for azimuthal anisotropy in the presence of gas bodies. Expanded Abstr., 88th Ann. Internat. SEG Mtg., Anaheim: 5123-5127.

Masmoudi, N. and Alkhalifah, T., 2018. Full-waveform inversion in acoustic ortho-rhombic media and application to a North Sea data set. Geophysics, 83(5): C179-C193.

Moradi, S. and Innanen, K.A., 2019. Azimuthally-dependent scattering potentials and full-waveform inversion sensitivities in low-loss viscoelastic orthorhombic media. J. Geophys. Engineer., 16: 367-388.

Moradi, S. and Innanen, K.A., 2017. Born scattering and inversion sensitivities in viscoelastic transversely isotropic media. Geophys. J. Internat., 211: 1177-1188.

Oh, J-W. and Alkhalifah, T., 2016. Elastic orthorhombic anisotropic parameter inversion: An analysis of parameterization. Geophysics, 81(6): C279-C293.

Oh, J-W. and Alkhalifah, T., 2019. Study on the full-waveform inversion strategy for 3D elastic orthorhombic anisotropic media: application to ocean bottom cable data. Geophys. Prosp., 67: 1219-1242.

Operto, S., Gholami, Y., Ribodetti, A., Brossier, R., Metivier, L., and Virieux, J., 2013. A guided tour of multiparameter full waveform inversion with multicomponent data: From theory to practice. The Leading Edge, 32: 1040-1054.

Pan, W., Innanen, K., Fehler, M., Margrave, G. and Fang, X., 2014. FWI inversion sensitivities of the elastic stiffness coefficients in fractured media: analytic results. CREWES Res. Report, 26.

Prieux, V., Brossier, R., Operto, S. and Virieux, J., 2013. Multiparameter full waveform inversion of multicomponent ocean-bottom-cable data from the Valhall field. Part 1: imaging compressional wave speed, density and attenuation. Geophys. J. Internat., 194: 1640-1664.

Plessix, R.-E. and Mulder, W.A., 2004. Frequency-domain finite-difference amplitude-preserving migration. Geophys. J. Internat., 157: 975-987.

Pratt, R.G., Shin, C. and Hicks, G.J., 1998. Gauss-Newton and full Newton methods in frequency-space seismic waveform inversion. Geophys. J. Internat., 133: 341-362.

Rodriguez-Herrera, A., Koutsabeloulis, N. and Zdraveva, O., 2014. Modeling orthorhombic velocity perturbations around salt domes in the Gulf of Mexico. Expanded Abstr., 84th Ann. Internat. SEG Mtg., Denver: 458-462.

Rocha, D., Tanushev, N. and Sava, P., 2017. Anisotropic elastic wavefield imaging using the energy norm. Geophysics, 82(3): S225-S234.

Rüger, A., 1997. P-wave reflection coefficients for transversely isotropic models with vertical and horizontal axis of symmetry. Geophysics, 62: 713-722.

Schoenberg, M. and Helbig, K., 1997. Orthorhombic media: Modeling elastic wave behavior in a vertically fractured earth. Geophysics, 62: 1954-1974.

Shaw, R.K. and Sen, M.K., 2004. Born integral, stationary phase and linearized reflection coefficients in weak anisotropic media. Geophys. J. Internat., 150: 225-238.

Singh, S., Tsvankin, I. and Zabihi Naeini, E., 2018. Bayesian framework for elastic full-waveform inversion with facies information. The Leading Edge, 37: 924-931.

Singh, S., Tsvankin, I. and Zabihi Naeini, E., 2020. Full-waveform inversion for elastic VTI media with borehole constraints. Geophysics, 85(6): R553-R563.

Singh, S., Tsvankin, I. and Zabihi Naeini, E., 2021. Elastic FWI for orthorhombic media with lithologic constraints applied via machine learning. Geophysics, 86(4): R589-R602.

Singh, S. and Tsvankin, I., 2020. Sensitivity analysis of FWI for elastic orthorhombic media. Expanded Abstr., 88th Ann. Internat. SEG Mtg., Houston: 171-175.

Song, X. and Alkhalifah, T., 2013. Modeling of pseudo-acoustic P-waves in orthorhombic media with a lowrank approximation. Geophysics, 74(4): C33-C40.

Tarantola, A., 1986. A strategy for nonlinear elastic inversion of seismic reflection data. Geophysics, 51: 1893-1903.

Tsvankin, I., 1997. Anisotropic parameters and P-wave velocity for orthorhombic media. Geophysics, 62: 1292-1309.

Tsvankin, I., 2012,. Seismic Signatures and Analysis of Reflection Data in Anisotropic Media, 3rd ed. SEG, Tulsa, OK.

Tsvankin, I. and Grechka, V., 2011. Seismology of Azimuthally Anisotropic Media and Seismic Fracture Characterization. SEG, Tulsa, OK.

Vasconcelos, I. and Tsvankin, I., 2006. Nonhyperbolic moveout inversion of wide azimuth P-wave data for orthorhombic media. Geophys. Prosp., 54: 535-552.

Vigh, D., Jiao, K., Watts, D. and Sun, D., 2014. Elastic full-waveform inversion application using multicomponent measurements of seismic data collection. Geophysics, 79(2): R63-R77.

Virieux, J. and Operto, S., 2009. An overview of full-waveform inversion in exploration geophysics. Geophysics, 74(6): WCC1-WCC26.

Wang, H. and Tsvankin, I., 2018. Methodology of waveform inversion for acoustic orthorhombic media. J. Seismic Explor., 27: 201-226.

Wang, X. and Tsvankin, I., 2013a. Multiparameter TTI tomography of P-wave reflection and VSP data. Geophysics, 78(5): WC51-WC63.

Wang, X. and Tsvankin, I., 2013b. Ray-based gridded tomography for tilted transversely isotropic media. Geophysics, 78(1): C11-C23.

Xie, Y., Zhou, B., Zhou, J., Hu, J., Xu, L., Wu, X., Lin, N., Loh, F-C., Liu, L. and Wang, Z., 2013. Orthorhombic full-waveform inversion for imaging the Luda field using wide-azimuth ocean-bottom-cable data. The Leading Edge, 36: 75-80.

APPENDIX

MOMENT TENSOR FOR ORTHORHOMBIC PARAMETER PERTURBATIONS

We consider an orthorhombic perturbation (layer) overlaid by a homogeneous VTI medium. The effective moment tensors corresponding to the stiffness perturbations (which depend on the velocities and density in our notation) can be computed as follows [see eq. (16)]:

$$\delta \mathbf{M_m} = \sum_{i,j} \frac{\partial C_{ij}}{\partial \mathbf{m}} \delta M_{ij} , \qquad (A\text{-}1)$$

where C_{ij} are the stiffness coefficients in the two-index (Voigt) notation, and $\mathbf{m}$ is the parameter vector of orthorhombic media.

Using eqs. (17) and (A-1), the moment tensors for the velocity-based parameterization [eqs. (12)-(14); the notation also includes the vertical velocities V_{P0} and $V_{S0}*$] can be found as:

$$\delta M_{V_{P0}} = 2\rho V_{P0} \begin{bmatrix} 0 & 0 & 0 \\ 0 & 0 & 0 \\ 0 & 0 & e_{33} \end{bmatrix} + q_1 \rho V_{P0} \begin{bmatrix} e_{33} & 0 & 0 \\ 0 & e_{33} & 0 \\ 0 & 0 & e_{11}+e_{22} \end{bmatrix}, \qquad (A\text{-}2)$$

$$\delta M_{V_{P1}} = 2\rho V_{\text{hor,P}} \begin{bmatrix} 0 & 0 & 0 \\ 0 & e_{22} & 0 \\ 0 & 0 & 0 \end{bmatrix}, \qquad (A\text{-}3)$$

$$\delta M_{V_{P2}} = 2\rho V_{\text{hor,P}} \begin{bmatrix} e_{11} & 0 & 0 \\ 0 & 0 & 0 \\ 0 & 0 & 0 \end{bmatrix} + q_2 \rho V_{\text{hor,P}} \begin{bmatrix} e_{22} & 0 & 0 \\ 0 & e_{22} & 0 \\ 0 & 0 & 0 \end{bmatrix}, \qquad (A\text{-}4)$$

$$\delta M_{V_{\text{nmo,1}}} = \frac{\rho V_{\text{nmo,P}}}{q_1} \begin{bmatrix} 0 & 0 & 0 \\ 0 & e_{33} & 0 \\ 0 & 0 & e_{22} \end{bmatrix}, \qquad (A\text{-}5)$$

$$\delta M_{V_{\mathrm{nmo},2}} = \frac{\rho V_{\mathrm{nmo,P}}}{q_1} \begin{bmatrix} e_{33} & 0 & 0 \\ 0 & 0 & 0 \\ 0 & 0 & e_{11} \end{bmatrix}, \tag{A-6}$$

$$\delta M_{V_{\mathrm{nmo},3}} = \frac{\rho V_{\mathrm{nmo,P}}}{q_2} \begin{bmatrix} e_{22} & 0 & 0 \\ 0 & e_{11} & 0 \\ 0 & 0 & 0 \end{bmatrix}, \tag{A-7}$$

$$\delta M_{V_{S0}} = 2\rho V_{S0} \begin{bmatrix} 0 & 0 & 2e_{13} \\ 0 & 0 & 0 \\ 2e_{13} & 0 & 0 \end{bmatrix} + \rho V_{S0}(q_1 + \frac{1}{q_1} + 2) \begin{bmatrix} -e_{33} & 0 & 0 \\ 0 & 0 & 0 \\ 0 & 0 & -e_{11} \end{bmatrix}, \tag{A-8}$$

$$\delta M_{V_{S1}} = 2\rho V_{S0} \begin{bmatrix} 0 & 0 & 0 \\ 0 & 0 & 2e_{23} \\ 0 & 2e_{23} & 0 \end{bmatrix} + \rho V_{S0}(q_1 + \frac{1}{q_1} + 2) \begin{bmatrix} 0 & 0 & 0 \\ 0 & -e_{33} & 0 \\ 0 & 0 & -e_{22} \end{bmatrix}, \tag{A-9}$$

$$\delta M_{V_{S2}} = 2\rho V_{\mathrm{hor,SH}} \begin{bmatrix} 0 & 2e_{12} & 0 \\ 2e_{12} & 0 & 0 \\ 0 & 0 & 0 \end{bmatrix} + \rho V_{\mathrm{hor,SH}}(q_2 + \frac{1}{q_2} + 2) \begin{bmatrix} -e_{22} & 0 & 0 \\ 0 & -e_{11} & 0 \\ 0 & 0 & 0 \end{bmatrix}, \tag{A-10}$$

$$\delta M_\rho =$$

$$V_{P0}^2 \begin{bmatrix} 0 & 0 & 0 \\ 0 & 0 & 0 \\ 0 & 0 & e_{33} \end{bmatrix} + V_{\mathrm{hor,P}}^2 \begin{bmatrix} e_{11} & 0 & 0 \\ 0 & e_{22} & 0 \\ 0 & 0 & 0 \end{bmatrix} + r_1 \begin{bmatrix} e_{22} & 0 & 0 \\ 0 & e_{11} & 0 \\ 0 & 0 & 0 \end{bmatrix} + r_2 \begin{bmatrix} e_{33} & 0 & 0 \\ 0 & e_{33} & 0 \\ 0 & 0 & e_{11} + e_{22} \end{bmatrix} +$$

$$V_{S0}^2 \begin{bmatrix} 0 & 0 & 2e_{13} \\ 0 & 0 & 2e_{23} \\ 2e_{13} & 2e_{23} & 0 \end{bmatrix} + V_{\mathrm{hor,SH}}^2 \begin{bmatrix} 0 & 2e_{12} & 0 \\ 2e_{12} & 0 & 0 \\ 0 & 0 & 0 \end{bmatrix}, \tag{A-11}$$

where

$$r_1 = \sqrt{(V_{\mathrm{hor},P}^2 - V_{\mathrm{hor},SH}^2)(V_{\mathrm{nmo},P}^2 - V_{\mathrm{hor},SH}^2)} - V_{\mathrm{hor},SH}^2 \,,$$

$$r_2 = \sqrt{(V_{P0}^2 - V_{S0}^2)(V_{\mathrm{nmo},P}^2 - V_{S0}^2)} - V_{S0}^2 \,,$$

$$q_1 = \sqrt{\frac{V_{P0}^2 - V_{S0}^2}{V_{\mathrm{nmo},P}^2 - V_{S0}^2}} \,, \text{ and } q_2 = \sqrt{\frac{V_{\mathrm{hor},P}^2 - V_{\mathrm{hor},SH}^2}{V_{\mathrm{nmo},P}^2 - V_{\mathrm{hor},SH}^2}} \,.$$

In the above equations, $V_{\mathrm{hor},P} = V_{P0}\sqrt{1+2\varepsilon}$, $V_{\mathrm{nmo},P} = V_{P0}\sqrt{1+2\delta}$, and $V_{\mathrm{hor},SH} = V_{S0}\sqrt{1+2\gamma}$ are the P-wave horizontal and NMO velocities and the SH-wave horizontal velocity, respectively, in the background VTI medium.